Theory and simulation of Ostwald ripening

Jian Hua Yao,* K. R. Elder, Hong Guo, and Martin Grant
Centre for the Physics of Materials, Physics Department, Rutherford Building, McGill University, 3600 rue University, Montréal, Québec, Canada H3A 2T8
(Received 17 August 1992; revised manuscript received 23 December 1992)

A theoretical approach to the Ostwald ripening of droplets is presented in dimension $D \geq 2$. A mean-field theory is constructed to incorporate screening effects in the competing many-droplet system. The mean-field equations are solved to infinite order in the volume fraction and provide analytic expressions for the coarsening rate, the time-dependent droplet-distribution function, and the time evolution of the total number of droplets. These results are in good agreement with experiments in three dimensions and with a very large scale and extensive numerical study in both two and three dimensions presented in this paper. The numerical study also provides the time evolution of the structure factors, which scale with the only length scale, the average droplet radius.

I. INTRODUCTION

When a binary mixture is cooled from a disordered phase into a two-phase metastable region (where the volume fraction ϕ of the minority component is small), the minority component condenses into spherical droplets. As time evolves, on average the droplets grow in radius $R(t)$, while their number decreases: Large droplets grow by the condensation of material diffused through the matrix from small evaporating droplets. This phenomenon is called Ostwald ripening. Figure 1 is a schematic picture of two-dimensional Ostwald ripening as time increases. In this figure, the shaded circles stand for the droplets fixed in two-dimensional space, and time evolves from (a) to (d). Figure 1 clearly shows that the small droplets are shrinking, while the large ones are growing; i.e., the large droplets are swallowing small ones. As time t evolves, the total number of droplets decreases and the average droplet radius increases, but the volume fraction of droplets ϕ (the shaded area) does not change with time. During the coarsening, the system tries to minimize its interfacial free energy by nonlocal diffusion. These are the main features of Ostwald ripening.

The theory of Ostwald ripening determines how the droplets evolve with time. Important quantities of interest are the droplet-distribution function $f(R,t)$, the average droplet radius $\overline{R}(t)$, and the total number of droplets, $N(t)$. The classic Ostwald-ripening theory is attributed to Lifshitz and Slyozov,[1] and Wagner[2] (LSW), who studied the case in which the volume fraction of the minority phase tends to zero, i.e., $\phi \to 0$, in dimension $D = 3$.

The starting point of the LSW theory is the diffusion equation for the concentration C in the steady-state limit:

$$\nabla^2 C(\mathbf{r}) = 0 \ , \tag{1}$$

where $\partial C/\partial t$ can be neglected. This determines the flow of material between droplets, subject to the Gibbs-Thomson boundary condition at the surface of a droplet of radius R:

$$C(r)\Big|_{r=R} = C_\infty \left(1 + \frac{\nu}{R}\right), \tag{2}$$

where ν is the capillary length, defined below, and the boundary condition far from all droplets:

$$\lim_{r\to\infty} C(\mathbf{r}) = \overline{C} \ , \tag{3}$$

where $\overline{C}$ is the mean concentration in the bulk. The

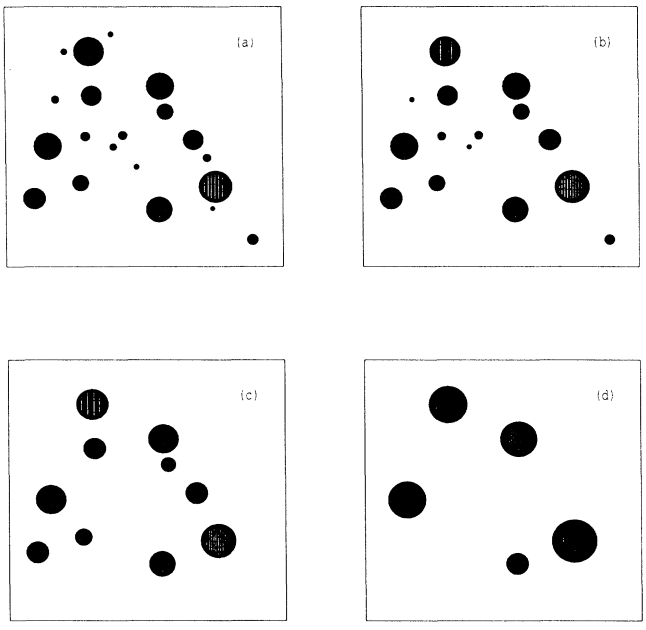

FIG. 1. This sketch shows the Ostwald-ripening phenomenon in two dimensions. The shaded circles represent the droplets (the minority component) fixed in two-dimensional space. As time evolves from (a) to (d), the total number of droplets decreases and the average droplet radius increases, but the volume fraction of droplets ϕ (the shaded area) is constant.

capillary length is $\nu = 2\gamma V_m C_\infty/(R_g T)$, where γ is the surface tension, V_m the molar volume, C_∞ the solute concentration at a flat interface, R_g the gas constant, and T the temperature. The mass balance

$$\frac{d}{dt}\left(\frac{4\pi}{3}R^3\right) = 4\pi R^2 \mathcal{D}\left.\frac{dC(r)}{dr}\right|_{r=R}, \tag{4}$$

where $\mathcal{D}$ is the diffusion constant, ensures that the changes in volume of the droplets, which are assumed to be spherical, are due to a change in concentration. The droplet-distribution function $f(R,t)$ determines averages by

$$\overline{(\cdots)} = \frac{\int dR\, f(R,t)\,(\cdots)}{\int dR\, f(R,t)} \tag{5}$$

with our convenient normalization

$$\int dR\, f(R,t) = N(t), \tag{6}$$

the total number of droplets. The distribution function obeys the continuity equation

$$\frac{\partial f(R,t)}{\partial t} + \frac{\partial}{\partial R}[\dot{R} f(R,t)] = 0\ ; \tag{7}$$

thus there is no source of new droplets (nucleation has ceased), where the overdot denotes a time derivative, and the conservation law

$$\Delta(t) + \frac{4\pi}{3}\int_0^\infty R^3 f(R,t) dR = Q\ , \tag{8}$$

where $\Delta(t) = \overline{C} - C_\infty$, is the supersaturation of the solution, which vanishes as $t \to \infty$; $Q = \phi V'$ is the initial concentration, and V' is the volume of the system. We shall consider this equation in the limit in which the minority phase (within the droplets) and majority phase (outside the droplets) are at their equilibrium concentrations, i.e., $\Delta(t) = 0$. These equations above follow for all small volume fractions, provided a steady-state droplet picture is reasonable.

In the limit of $\phi \to 0$, the solution of the steady-state diffusion equation is

$$C(r) = \overline{C} - [\overline{C} - C(R)]R/r\ , \tag{9}$$

since one need only consider one droplet. With the equation for mass balance, this gives the growth law in that limit:

$$\frac{dR}{dt} = \frac{\mathcal{D}}{R}\left(\Delta - \frac{\nu}{R}\right)\ , \tag{10}$$

where, evidently, droplets larger (smaller) than the time-dependent critical radius $\nu/\Delta(t)$ grow (shrink). In an elegant calculation, LSW determined the asymptotic growth rate of the average droplet radius to be

$$\overline{R}(t) = \left(\frac{4\mathcal{D}\nu t}{9}\right)^{1/3}, \tag{11}$$

where the prefactor 4/9 is the dimensionless coarsening rate, and the overbar denotes an average. In addition to this prediction, an analytic form for the droplet distribution function was obtained:

$$f(R,t) \propto g(R/\overline{R})/\overline{R}^4 \tag{12}$$

for late times. The explicit form of the scaled normalized distribution function is

$$g(z) = \begin{cases} (3^4 e/2^{5/3}) z^2 \exp[-1/(1-\frac{2}{3}z)]/[(z+3)^{7/3}(\frac{3}{2}-z)^{11/3}] & \text{if } 0 < z < \frac{3}{2}, \\ 0 & \text{otherwise.} \end{cases} \tag{13}$$

This important work revealed both power-law growth and dynamic scaling, which are now considered universal characteristics of the kinetics of a first-order phase transition.[3]

Nevertheless, it has proved difficult to test their theory rigorously by experiment or numerical simulation. Experiments typically study volume fractions appreciably larger than zero, and large-scale numerical work has been limited by previous computer facilities. Earlier work on extending the theory of LSW to nonzero ϕ has been attempted by many groups,[4–13] using both analytic and numerical methods.

For the most part, analytic extensions have been based either on *ad hoc* assumptions (the work of Ardell[9] and Tsumuraya and Miyati[10]), or on perturbative expansions in ϕ, typically taken to order $\sqrt{\phi}$ [the work of Marqusee and Ross[4] (MR) and Tokuyama, Kawasaki, and Enomoto[5] (TKE)]. In addition, an ambitious theory was developed by Mardar[12] in which two-particle correlations were included for three-dimensional Ostwald ripening. All these approaches lead to the following growth law:

$$\overline{R}(t) = [\overline{R}^3(0) + K(\phi)t]^{1/3}, \tag{14}$$

where the coarsening rate $K(\phi)$ is a monotonically increasing function of ϕ. The droplet-distribution function satisfies

$$f(R,t) \propto g(z,\phi)/\overline{R}^{(D+1)}\ , \tag{15}$$

where $z \equiv R/\overline{R}$. The theories predict a broadening of $g(z,\phi)$ as the volume fraction is increased. Unfortunately, the perturbative theories can neither go beyond $\mathcal{O}(\sqrt{\phi})$ nor be applied to two-dimensional systems, and the *ad hoc* approaches contain uncontrolled approximations. Indeed, in many cases the theories for $D = 3$ give rather different results, as we shall show below. Experiments are not of sufficient quality to distinguish them.

To our knowledge, two numerical studies have been conducted in three dimensions. In 1984, Voorhees and Glicksman[7] (VG) carried out a numerical simulation, by a very interesting novel approach based on Ewald-sum techniques, reviewed below. Unfortunately that work was hampered by the computing facilities available at that time, and the number of droplets included was too few to give conclusive results. More recently Beenakker[8] attempted to extend their work, but he only included a rather small number (≈ 20) of nearest-neighbor interactions. Thus, in his simulation, the volume fraction was not fixed, and drifted 10–20 %. Thus neither work provided a good test for theory.

For two-dimensional systems, theory has been hampered by the logarithmic divergence present in the steady-state limit of the two-dimensional diffusion equation. Marqusee[15] proposed a self-consistent theory, which Zheng and Gunton[16] extended by including two-particle correlations. However, Marqusee's two-dimensional theory is very different from his three-dimensional theory with Ross,[4] while Zheng and Gunton's theory involved numerous approximations following Mardar's theory. Recently Ardell[9] published an extension to two dimensions of his phenomenological theory for three-dimensional coarsening. His theory, however, involves an *ad hoc*, although physically motivated, free parameter. These groups obtain the growth law and scaling function as for three dimensions [Eqs. (14) and (15) above]. A different result was obtained in the non-steady-state calculation for $\phi \to 0$ by Rogers and Desai[17] (RD). They found scaling with $\overline{R} \sim (t/\ln t)^{1/3}$, for that limit in $D = 2$. Up to now, there have been no experiments to test these theories, which have rather different predictions, although numerical work on a nonlinear Langevin equation has been done by Toral, Chakrabarti, and Gunton.[18]

In summary, although a great deal of progress has been made in understanding Ostwald ripening, a fully satisfactory approach has not yet been found, and it has remained a vexing problem in the field. Thus, we felt it worthwhile to reinvestigate this fundamental phenomenon.[13] The goal of this article is to present a systematic method to study Ostwald ripening in $D \geq 2$ at nonzero volume fractions (for simplicity, ϕ will be called the volume fraction, although, for example, in $D = 2$ it is an area fraction). To do so, we have introduced a mean-field model that we solve exactly in arbitrary dimension. We then test our results by comparison to an experiment in three dimensions, and to a large-scale simulation we have done in two and three dimensions. This numerical simulation also provides an estimate of the dynamic structure factor, which we find obeys a dynamic scaling relationship.

The organization of the paper is as follows: In Sec. II we introduce a Thomas-Fermi-type approximation to reduce the steady-state many-body diffusion equation to a set of one-body diffusion equations, where the conservation law plays the role of charge neutrality. Applying the Gibbs-Thomson condition to these solutions and using the conservation law, we obtain the basic equations of our mean-field theory. Section III presents the solution of the basic equations. In Sec. IV formulas for both two- and three-dimensional numerical simulations are derived by means of the Ewald technique.[19] Section V presents the simulation results and compares them with those of our mean-field theory, previous theories, and an experiment in three dimensions. A short conclusion to this article is given in Sec. VI.

II. MEAN-FIELD THEORY

Our study makes use of dimensionless variables. Units of length and time are given in terms of a characteristic length $l_c = (D-1)\gamma V_m/R_gT$ and a characteristic time $t^* = l_c^2/(\mathcal{D}C_\infty V_m)$. It is also convenient to introduce a dimensionless concentration field $\theta(\mathbf{r}) = [C(\mathbf{r}) - C_\infty]/C_\infty$. All the quantities involved have been defined in Sec. I.

The many-droplet diffusion problem is intractable without approximation. In the steady-state limit, the fundamental equation is[7]

$$\nabla^2\theta(\mathbf{r}) = a\sum_{i=1}^{N} B_i\delta(\mathbf{r}-\mathbf{r}_i), \tag{16}$$

where N is the number of the droplets in the system, $a = 2\pi^{D/2}/\Gamma(D/2)$, $\mathbf{r}_i$ gives the location of the ith droplet, and B_i is the strength of the source or sink of current for diffusion. This is the multidroplet diffusion equation in the quasistationary approximation, where $\partial\theta/\partial t$ is neglected because the growth rate of droplets is much slower than the relaxation time of concentration field in the matrix. The δ functions on the right-hand side of Eq. (16) result from the assumption that the droplet locations remain fixed in space and the distances between droplets are much larger than the average droplet radius. This is a very good description for systems with small volume fractions. The necessary boundary conditions are the Gibbs-Thomson condition for the concentration field at the curved surface of each droplet and the imposed supersaturation far from all droplets:

$$\theta(\mathbf{r})|_{|\mathbf{r}-\mathbf{r}_i|=R_i} = \frac{1}{R_i} \quad \text{and} \quad \lim_{r\to\infty}\theta(\mathbf{r}) = \theta_{\text{av}} \tag{17}$$

for $i = 1,\ldots,N$, where θ_{av} is the average concentration outside the droplets. The conservation law is

$$\sum_{i=1}^{N} B_i = 0\ , \tag{18}$$

which implies that we shall consider the limit in which the minority phase (within the droplets) and majority phase (outside the droplets) are at their equilibrium concentrations,[7] and the growth law satisfies

$$\frac{d(vR_i^D)}{dt} = -\int_{s_i}\mathbf{J}\cdot\mathbf{n}\,d\sigma\ , \tag{19}$$

where s_i is surface of the ith droplet, $\mathbf{n}$ is the unit vector normal to the droplet surface, and $v = \pi^{D/2}/\Gamma(D/2+1)$. Substituting the Fourier-Fick law $\mathbf{J} = -\nabla\theta$ into Eq. (19) and transforming the surface integral over the ith droplet into a volume integral gives

$$\frac{d(vR_i^D)}{dt} = \int \nabla^2\theta \, dv \ . \tag{20}$$

The explicit form of the growth law can then be obtained by substituting Eq. (16) in Eq. (20), i.e.,

$$\frac{dR_i}{dt} = \frac{B_i}{R_i^{D-1}}. \tag{21}$$

LSW made a mean-field approximation in the limit of $\phi \to 0$ to solve these equations. For nonzero ϕ we shall make use of the fact that the steady-state problem resembles a homogeneous electron gas since droplets interact via the Laplace equation in the steady-state limit and charge neutrality is invoked through Eq. (18). We introduce screening effects among the droplets and approximate the many-droplet correlation effects in the same manner as the Thomas-Fermi mechanism for Coulomb systems. Within a mean-field approximation, the change in volume of a droplet only depends on the concentration gradients set up by each droplet:

$$\frac{d(vR_i^D)}{dt} = \sum_{R_j} I_{\rm int}(R_i, R_j)[\theta_{\rm av} - \theta(R_j)], \tag{22}$$

where $I_{\rm int}(R_i, R_j)$ is the interaction matrix which is yet to be determined. However, since we shall assume all droplets are equivalent, one may simply make the approximation $I_{\rm int}(R, R') \approx I(R)\delta_{R,R'}$. Hence, based on a mean-field approximation, the growth law must obey

$$\frac{d(vR_i^D)}{dt} = I(R_i)[\theta_{\rm av} - \theta(R_i)], \tag{23}$$

assuming spherical growth. The mean-field approximation results from the assumption that the flux determining the growth rate for each droplet is only proportional to the difference between the boundary concentration and the *average* bulk concentration. The curvature-dependent rate coefficient $I(R)$ is unknown *a priori*, but will be determined self-consistently in terms of a screening length below.

From Eq. (8), the average bulk concentration field then obeys[20]

$$\begin{aligned}\frac{\partial\theta_{\rm av}}{\partial t} &= -\frac{1}{V'}\frac{\partial}{\partial t}\int_0^\infty f(R,t) v R^D dR \\ &= -\frac{1}{V'}\int_0^\infty \frac{d(vR^D)}{dt} f(R,t) dR \ ,\end{aligned} \tag{24}$$

where we used the continuity Eq. (7) and carried out integration by parts, and V' is the system volume. By substituting Eq. (23) into Eq. (24), we obtain

$$\begin{aligned}\frac{\partial\theta_{\rm av}}{\partial t} = &-\frac{1}{V'}\int_0^\infty I(R)\theta_{\rm av} f(R,t) dR \\ &+\frac{1}{V'}\int_0^\infty I(R)\theta(R) f(R,t) dR.\end{aligned} \tag{25}$$

We now postulate an equation of motion for the local concentration field $\theta(\mathbf{r}, t)$ in the vicinity of the ith droplet. The simplest form it can satisfy is

$$\frac{\partial\theta}{\partial t} = \nabla^2\theta - \xi^{-2}\theta + S - aB_i\delta(\mathbf{r} - \mathbf{r}_i). \tag{26}$$

Here we have approximated the contribution from other droplets in Eq. (16) through the introduction of a screening length ξ and a source or background field $S\xi^2$. We shall now self-consistently relate these quantities to $I(R)$ by integrating the equation above and comparing it with Eq. (25), i.e.,

$$\xi^{-2} = \frac{1}{V'}\int_0^\infty I(R) f(R,t) dR \tag{27}$$

and

$$S = \frac{1}{V'}\int_0^\infty I(R)\theta(R) f(R,t) dR. \tag{28}$$

Equations (23) and (26) completely specify our mean-field approximation; indeed, they are the only approximations needed to solve the equations in the steady-state limit. Their form implies we consider a one-body problem without correlations. A systematic derivation of these equations from first principles would be valuable, since corrections to our equations, involving correlations, could be calculated. However, we have not been able to obtain such a derivation, although, as we have indicated above, a coarse graining of the microscopic equations, with the requirement that only a one-body distribution function is involved, will lead to our self-consistent starting point.

In the steady-state limit, the concentration field obeys

$$\nabla^2\theta - \xi^{-2}\theta + \xi^{-2}\theta_{\rm av} = aB_i\delta(\mathbf{r} - \mathbf{r}_i) \tag{29}$$

in the vicinity of the ith droplet.[13,14] The solution of Eq. (29) at the boundary ($|\mathbf{r} - \mathbf{r}_i| = R_i$) is then

$$\frac{1}{R_i} = \theta_{\rm av} - B_i V(R_i/\xi, R_i) \tag{30}$$

for $i = 1, \ldots, N$, where $V(R/\xi, R)$ is the Green's function of Eq. (29). In $D = 3$, $V(R/\xi, R) = \exp(-R/\xi)/R$; in $D = 2$, $V(R/\xi, R) = K_0(R/\xi)$, where K_0 is the zeroth-order modified Bessel function. Equations (30) and (18) can then be used to solve for B_i and $\theta_{\rm av}$. Substituting these solutions into Eq. (21) gives

$$\frac{dR}{dt} = \frac{R^{1-D}}{V(R/\xi, R)}\left\{\frac{\overline{[RV(R/\xi,R)]^{-1}}}{\overline{[V(R/\xi,R)]^{-1}}} - \frac{1}{R}\right\}, \tag{31}$$

where the overbar is defined as

$$\overline{A} \equiv \int_0^\infty A f(R,t) dR \Big/ \int_0^\infty f(R,t) dR \ . \tag{32}$$

Comparing Eq. (31) with Eq. (23) gives $I(R) = a/V(R/\xi, R)$, so that

$$\xi^{-2} = \frac{a}{V'}\int_0^\infty f(R,t)/V(R/\xi,R) dR. \tag{33}$$

The conservation law Eq. (18) can be rewritten as

$$\frac{v}{V'}\int_0^\infty R^D f(R,t) dR = \phi. \tag{34}$$

Equations (7), (31), (33), and (34) form the basic equations of our mean-field theory.

III. SOLUTION OF MEAN-FIELD-THEORY EQUATIONS

Equations (7), (31), (33), and (34) are integrable, and can be solved straightforwardly. First, we make the scaling *ansatz* $f(R,t) = H(t)G[R/u(t)]$, where u and H are arbitrary functions of t. The only scaling form of $f(R,t)$ that can satisfy this relationship and Eq. (34) is then

$$f(R,t) = \frac{\phi V'}{v\int_0^\infty x^D G(x)dx}\frac{G(x)}{u^{D+1}(t)}, \tag{35}$$

where $x = R/u(t)$. By making the transformation $\xi = \eta u(t)$ and inserting Eq. (35) into Eq. (33), we obtain

$$\eta^{-2} = \frac{\phi D}{\int_0^\infty x^D G(x)dx}\int_0^\infty \frac{G(x)}{V(x/\eta,x)}dx. \tag{36}$$

By using Eq. (35), the partial derivative of f with respect to time can be written as

$$\frac{\partial f(R,t)}{\partial t} = -\frac{C_0}{u^{D+2}(t)}\frac{du(t)}{dt}\left\{DG(x) + \frac{d}{dx}[xG(x)]\right\}, \tag{37}$$

where $C_0 = \phi V'/[v\int_0^\infty x^D G(x)dx]$. The second term on the right-hand side of Eq. (7) can be obtained from Eqs. (35) and (31), i.e.,

$$\frac{\partial}{\partial R}[\dot{R}f(R,t)] = \frac{C_0}{u^{D+4}(t)}\frac{d}{dx}\left[\frac{x^{1-D}}{V(x/\eta,x)}\left(\sigma - \frac{1}{x}\right)G(x)\right], \tag{38}$$

where

$$\sigma = \int_0^\infty G(x)[xV(x/\eta,x)]^{-1}dx \Big/ \int_0^\infty G(x)V^{-1}(x/\eta,x)dx. \tag{39}$$

Substituting Eqs. (37) and (38) into Eq. (7) gives the following first-order separable partial differential equation:

$$u^2(t)\frac{du(t)}{dt} = \frac{\frac{d}{dx}[x^{1-D}(\sigma - 1/x)/V(x/\eta,x)G(x)]}{DG(x) + \frac{d}{dx}[xG(x)]} = \lambda, \tag{40}$$

where the time-independent separation factor λ implicitly depends on ϕ. Finally by introducing the function

$$w(x,\lambda) = x^{1-D}(\sigma - x^{-1})/V(x/\eta,x) - \lambda x, \tag{41}$$

Eq. (40) can be split into two differential equations as follows:

$$u^2(t)\frac{du(t)}{dt} = \lambda \tag{42}$$

and

$$G(x) = \frac{1}{\lambda D}\frac{d}{dx}[w(x)G(x)]. \tag{43}$$

The solution of Eq. (42) is

$$u(t) = [u^3(0) + 3\lambda t]^{1/3}, \tag{44}$$

and the normalized solution of Eq. (43) is

$$G(x) = \frac{-\lambda D}{w(x,\lambda)}\exp\left(\lambda D\int_0^x w^{-1}(x',\lambda)dx'\right), \tag{45}$$

or the trivial solution $G(x) = 0$.

To determine the separation factor λ, we first note that both $G(x)$ and λ are positive. Equation (45) then demands that $w(x,\lambda)$ be negative. However, the asymptotic behavior of $V(x/\eta,x)$ implies that $\lim_{x\to\infty} w(x,\lambda) = +\infty$. Thus, there must exist an upper bound x_0 such that Eq. (45) is valid for $0 < x < x_0$ and the trivial solution $G(x) = 0$ is valid for $x \geq x_0$, i.e.,

$$G(x) = \begin{cases} \frac{-D\lambda}{w(x,\lambda)}\exp[D\lambda\int_0^x w^{-1}(x',\lambda)dx'] & \text{if } 0 < x < x_0, \\ 0 & \text{otherwise}, \end{cases} \tag{46}$$

and

$$w(x_0,\lambda) = 0\,. \tag{47}$$

Furthermore, from Eq. (43), it can be shown by induction that $G(x)$ is an analytic function of x since $w(x,\lambda)$ is an analytic function of x. If $w'(x_0,\lambda) \neq 0$, $G(x)$ is nonanalytic at $x = x_0$ (see Appendix A); thus

$$w'(x_0,\lambda) = 0\,. \tag{48}$$

Equations (47) and (48) completely determine the parameters λ and x_0.

The classic results of LSW can be recovered by considering the limit $\phi \to 0$ or $\eta \to \infty$. In this limit, Eq. (41) reduces to

$$w(x,\lambda) = \frac{1}{x}\left(\sigma - \frac{1}{x}\right) - \lambda x\,. \tag{49}$$

The parameters x_0, λ, and σ can then be obtained using this result along with Eqs. (47) and (48) [which imply $w(x,\lambda) = (x - x_0)^2 f(x)$]. These restrictions lead to the following form for w:

$$w(x,\lambda) = -\frac{4}{27x^2}(x+3)(x-3/2)^2\,, \tag{50}$$

i.e., $\sigma = 1$, $\lambda = 4/27$, and $x_0 = 3/2$. Substituting these quantities into Eq. (46) and carrying out the integration gives

$$G(x) = \begin{cases} Cx^2\exp\left(\frac{D/2}{x-3/2}\right)\Big/[(3/2-x)^{2+5D/9}(x+3)^{1+4D/9}] & \text{if } 0 < x < \frac{3}{2}, \\ 0 & \text{otherwise}, \end{cases} \tag{51}$$

where $C = D3^D e^{D/3}/2^{5D/9}$. For $D = 3$, Eq. (51) recovers the LSW distribution function given in Eq. (13).

The two-dimensional case must be treated differently since $K_0(x/\eta)$ has a logarithmic singularity as ϕ goes to zero, i.e., $\lim_{\phi\to 0} K_0(x/\eta) = \ln \phi^{-1/2}$. In this limit, Eq. (40) can be split into two differential equations as follows:

$$\ln \phi^{-1/2} u^2(t) \frac{du(t)}{dt} = \lambda \tag{52}$$

and

$$G(x) = \frac{1}{D\lambda} \frac{d}{dx}[w(x,\lambda)G(x)] \ , \tag{53}$$

where $w(x,\lambda)$ is identical to Eq. (49). The solution of Eq. (52) is

$$u(t) = [u^3(0) + 3\lambda t/\ln(\phi^{-1/2})]^{1/3} \ , \tag{54}$$

and the solution of Eq. (53) is the same as Eq. (51). Equation (51) in $D = 2$ is actually the same as the non-steady-state result of RD (Ref. 17) for $\phi \to 0$, but it differs from the two-dimensional theories of Marqusee[15] and Zheng and Gunton.[16] A comparison with their theories will be given later.

For larger values of ϕ (up to a limit discussed below), we have numerically solved Eqs. (47) and (48) self-consistently for x_0 and λ. The procedure for determining the various quantities needed to evaluate $\overline{R}$ and $g(z,\phi)$ can be summarized as follows. In $D = 3$, Eqs. (47) and (48) can be reduced to

$$x_0 = \frac{6}{2\sigma + \frac{1}{\eta} + \sqrt{(2\sigma - \frac{1}{\eta})^2 - 4\frac{\sigma}{\eta}}} \tag{55}$$

and

$$\lambda = (\sigma x_0 - 1) \exp\left(\frac{x_0}{\eta}\right) / x_0^3 \ . \tag{56}$$

An initial guess for σ and η is made and then Eqs. (36), (39), (46), (55), and (56) are used to compute new values of σ and η. This calculation is repeated until σ and η no longer change. Similar calculations can be performed in other dimensions.

To compare with other theories and experiments, it is convenient to use the conventional variable $z = R/\overline{R}$ as the argument of the scaled distribution function and to define the scaled distribution function as $g(z) = x_{\rm av} G(x_{\rm av} z)$, i.e.,

$$g(z) = \begin{cases} \frac{-D\lambda x_{\rm av}}{w(x_{\rm av} z,\lambda)} \exp(D\lambda \int_0^{x_{\rm av} z} w^{-1}(z',\lambda) dz') & \text{if } 0 < z < z_0 \\ 0 & \text{otherwise} \ , \end{cases} \tag{57}$$

where $z_0 = x_0/x_{\rm av}$ and $x_{\rm av} = \int_0^\infty x G(x) dx$.

The average radius of the droplets, $\overline{R}(t)$, and the total number of the droplets, $N(t)$, can now be calculated. From the definition given in Eq. (32), $\overline{R}(t)$ becomes

$$\overline{R}(t) = [\overline{R}^3(0) + K(\phi)t]^{1/3} \ , \tag{58}$$

where $K(\phi) = 3\lambda x_{\rm av}^3$. Equation (58) indicates that the coarsening exponent is universal and dimension independent. For $\phi \to 0$ in $D = 3$, Eq. (58) becomes $\overline{R}(t) = [\overline{R}^3(0) + 4t/9]^{1/3}$, recovering the LSW result given in Eq. (11). In $D = 2$, the growth law takes the form $\overline{R}(t) = [\overline{R}^3(0) + 4x_{\rm av}^3 t/(9 \ln \phi^{-1/2})]^{1/3}$. The logarithmic singularity in the growth rate implies that there is no consistent steady-state result in $D = 2$ for $\phi = 0$. In this limit Rogers and Desai[17] obtained the *non*-steady-state result $\overline{R} \sim (t/\ln t)^{1/3}$ and the same distribution function as Eq. (51). Finally, within our model, the time evolution of the number of the droplets is

$$N(t) = \int_0^\infty f(R,t) dR = \frac{N(0)\overline{R}^D(0)}{[\overline{R}^3(0) + K(\phi)t]^{D/3}} \ . \tag{59}$$

Figure 2 shows the droplet-distribution function for $\phi \to 0$ in $D = 2$, 3, 4, and 5, which indicates that, in the limit $\phi \to 0$, a higher-dimensional distribution function is broader than a lower-dimensional one. This phenomenon can be understood by examining Eq. (31). In this limit, except $D = 2$, Eq. (31) can be reduced to

$$\frac{dR}{dt} = \frac{1}{R}\left(\frac{x_{\rm av}}{\overline{R}} - \frac{1}{R}\right) \ . \tag{60}$$

From Eq. (51), $x_{\rm av}$ is a monotonically decreasing function of dimensions D; therefore, the critical radius $R_c =$

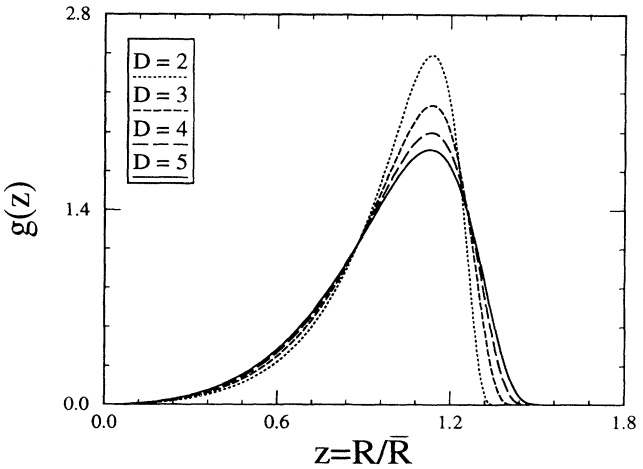

FIG. 2. Comparison of scaled normalized distribution functions $g(z)$ vs scaled droplet radius $z = R/\overline{R}$ for $\phi \to 0$ in $D = 2$, 3, 4, and 5.

$\overline{R}/x_{\rm av}$ increases with dimensions D. As a result, more droplets shrink and less droplets grow in higher dimensions than in lower dimensions. In addition to the conservation law, the growing droplets in higher dimensions grow faster than those in lower dimensions on average, which results in a broader range distribution function for higher dimensions.

Figure 3 presents the finite-volume-fraction effects on our theoretical scaled normalized distribution function Eq. (57) for both $D = 2$ and $D = 3$. It indicates that the distribution function is sensitive to ϕ. As ϕ increases, $g(z, \phi)$ becomes broader. This phenomenon can also be easily understood by examining Eq. (31). In three dimensions, for instance, Eq. (31) can be reduced to

$$\frac{dR}{dt} = \frac{\exp(R/\xi)}{R}\left(\frac{\sigma}{u(t)} - \frac{1}{R}\right). \tag{61}$$

According to our numerical calculations, the screening length obeys $\xi \sim \overline{R}/\sqrt{3\phi}$, and the critical radius $R_c = u(t)/\sigma$ is insensitive to the volume fraction ϕ, compared to $\exp(R/\xi)$. Consequently, as ϕ increases, the droplets whose radii are greater than the critical radius grow faster, and the droplets whose radii are smaller than the critical radius shrink faster, which leads to a broader droplet distribution. Comparisons of our prediction for $g(z)$ with an experimental result, simulations, and other theories will be presented in Sec. V.

Figure 4 displays the relation between the scaled screening length and the volume fraction: In $D = 2$, our scaled screening length is almost the same as Marqusee's; in $D = 3$, ours is close to that of both MR and TKE.

Our theory is inapplicable to large volume fractions where the screening length ξ is close to the average radius of the droplets $\overline{R}$ since a Thomas-Fermi approximation is made and the droplets are treated as point sources and sinks. Indeed, there is no solution for Eqs. (36), (39), (46), (47), and (48) if $\xi < 2.7\overline{R}$ for $D = 2$ and $\xi < 1.9\overline{R}$ for $D = 3$, corresponding to $\phi > 0.085$ and $\phi > 0.06$, respectively. This can be easily seen in $D = 3$. As ϕ increases, η decreases such that Eq. (47) has no real solutions (since σ is of the order one). This unphysical solution gives a self-consistent criteria for the applicability of our approach.

Finally, we note that although our straightforward ap-

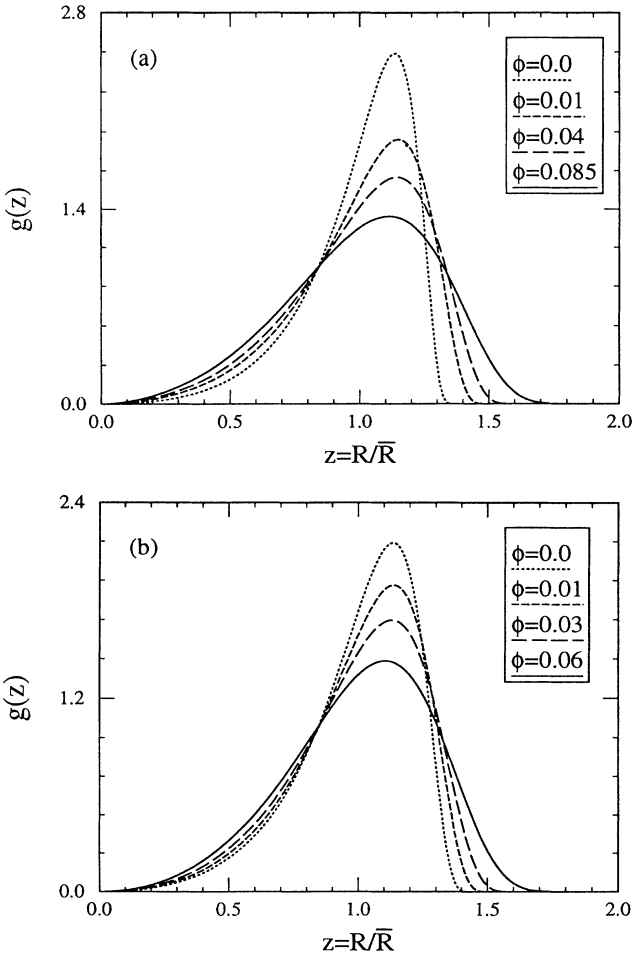

FIG. 3. Predictions of our theory for the scaled normalized distribution $g(z)$ [Eq. (57)] vs scaled droplet radius $z = R/\overline{R}$ are displayed for different volume fractions. (a) and (b) display $g(z)$ for $D = 2$ and $D = 3$, respectively.

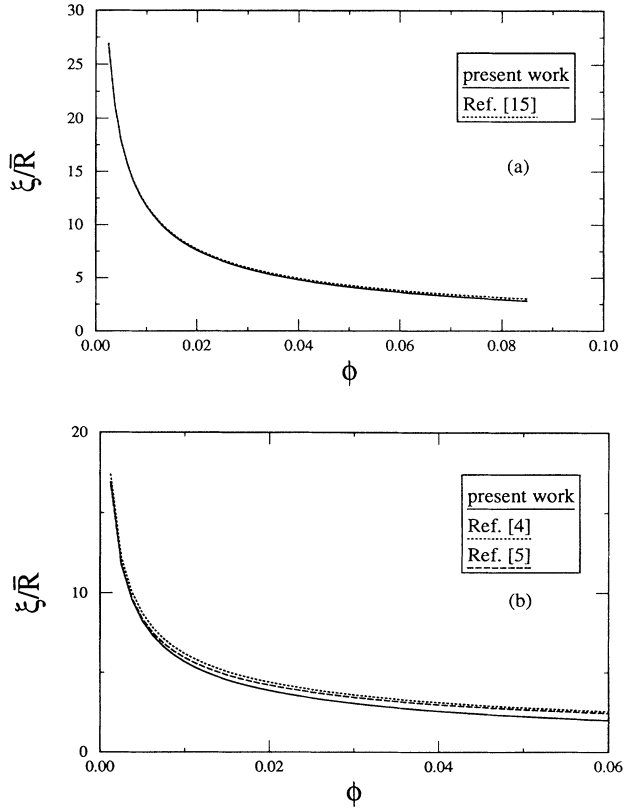

FIG. 4. In this figure, the scaled screening length $\xi/\overline{R}$ is displayed as a function of ϕ. The dotted and solid lines in (a) correspond to the results of Marqusee (Ref. 15) and ours, respectively, in $D = 2$; the dotted, dashed, and solid lines in (b) correspond, respectively, to the results of MR (Ref. 4), TKE (Ref. 5), and ours.

proach is quite different from those of MR and TKE, our results for $K(\phi)$ and $g(z)$ are indistinguishable from theirs to order of $\mathcal{O}(\sqrt{\phi})$.

IV. BASIC EQUATIONS FOR NUMERICAL SIMULATIONS

To test our mean-field theory results of the preceding section, we have undertaken a numerical simulation similar to that of VG.[7] To derive the basic equations of our simulation, we first start from the solution of Eq. (16) in three dimensions, i.e.,

$$\theta(\mathbf{r}) = B_0 - \sum_{i=1}^{N} \frac{B_i}{|\mathbf{r}-\mathbf{r}_i|} , \tag{62}$$

where B_0 is an integration constant which, in general, is nonzero.

The Gibbs-Thomson boundary condition then becomes

$$\frac{1}{R_j} = B_0 - \sum_{i=1}^{N} \frac{B_i}{|\mathbf{r}_i - \mathbf{R}_j|} , \tag{63}$$

where $\mathbf{R}_j$ is a position vector of the jth droplet's boundary, and $R_j = |\mathbf{R}_j - \mathbf{r}_j|$ is the jth droplet's radius. If we define ψ_{ji} as the angle between vectors $(\mathbf{R}_j - \mathbf{r}_j)$ and $(\mathbf{r}_j - \mathbf{r}_i)$, Eq. (63) can be written as

$$\frac{1}{R_j} = B_0 - \frac{B_j}{R_j} - \sum_{i=1,i\neq j}^{N} \frac{B_i}{\sqrt{(\mathbf{r}_i-\mathbf{r}_j)^2 + R_j^2 - 2R_j|\mathbf{r}_i-\mathbf{r}_j|\cos\psi_{ji}}} . \tag{64}$$

Finally, we make a monopolar approximation to remove the dependence on ψ_{ji} from Eq. (64). This approximation assumes that all the other droplets are distributed randomly around the jth so that ψ_{ji} can be averaged over. Averaging both sides of Eq. (64) with respect to the polar angle ψ_{ji} and the azimuthal angle φ , due to the fact that

$$\frac{1}{4\pi}\int_0^{\pi}\int_0^{2\pi} \frac{\sin\psi_{ji}\, d\psi_{ji} d\varphi}{\sqrt{(\mathbf{r}_i-\mathbf{r}_j)^2 + R_j^2 - 2R_j|\mathbf{r}_i-\mathbf{r}_j|\cos\psi_{ji}}} = \frac{1}{|\mathbf{r}_i-\mathbf{r}_j|} , \tag{65}$$

Eq. (64) becomes

$$\frac{1}{R_j} = B_0 - \frac{B_j}{R_j} - \sum_{i=1,i\neq j}^{N} \frac{B_i}{|\mathbf{r}_j-\mathbf{r}_i|} . \tag{66}$$

This monopolar approximation was also adopted by VG (Ref. 7) and Beenakker.[8] Equation (66), the conservation law, Eq. (18), and the three-dimensional version of growth law, Eq. (21), form the basic equations of the three-dimensional simulations. Although VG (Ref. 7) used a different form of Eq. (66) in their simulation, our numerical tests have shown that the relative difference between our growth rates $\{B_i\}$ and theirs is of order of 10^{-4} for droplet numbers from 100 to 1000. We believe, therefore, that our basic equations are essentially the same as those of VG.

Similarly, the solution of Eq. (16) in two dimensions is

$$\theta(\mathbf{r}) = B_0 + \sum_{i=1}^{N} B_i \ln|\mathbf{r}-\mathbf{r}_i| . \tag{67}$$

The Gibbs-Thomson boundary condition then becomes

$$\frac{1}{R_j} = B_0 + B_j \ln|\mathbf{R}_j - \mathbf{r}_j| + \sum_{i=1,i\neq j}^{N} B_i \ln|\mathbf{R}_j - \mathbf{r}_i| . \tag{68}$$

Similar to three dimensions, Eq. (68) can be written as

$$\frac{1}{R_j} = B_0 + B_j \ln R_j + \sum_{i=1,i\neq j}^{N} B_i \ln|\mathbf{r}_j-\mathbf{r}_i| + \sum_{i=1,i\neq j}^{N} B_i \ln\left(1 - \frac{2R_j}{|\mathbf{r}_j-\mathbf{r}_i|}\cos\varphi_{ji} + \frac{R_j^2}{|\mathbf{r}_j-\mathbf{r}_i|^2}\right)^{1/2} . \tag{69}$$

By means of the monopolar approximation, Eq. (69) can be reduced to

$$\frac{1}{R_j} = B_0 + B_j \ln R_j + \sum_{i=1,i\neq j}^{N} B_i \ln|\mathbf{r}_j-\mathbf{r}_i| . \tag{70}$$

To provide equations suitable for numerical simulation in two dimensions, some manipulations of our fundamental equations are needed. To do so, we split θ into two pieces, i.e., $\theta = \theta_1 + \theta_2$, such that θ_1 and θ_2 are solutions of the following equations:

$$\nabla^2\theta_1(\mathbf{r}) = -2\pi\rho_1(\mathbf{r}) \tag{71}$$

and

$$\nabla^2\theta_2(\mathbf{r}) = -2\pi\rho_2(\mathbf{r}) , \tag{72}$$

where

$$\rho_1(\mathbf{r}) = -\frac{\eta}{\pi}\sum_{i=1}^{N} B_i \exp[-\eta|\mathbf{r}-\mathbf{r}_i|^2] , \tag{73}$$

$$\rho_2(\mathbf{r}) = \frac{\eta}{\pi}\sum_{i=1}^{N} B_i \exp[-\eta|\mathbf{r}-\mathbf{r}_i|^2] - \sum_{i=1}^{N} B_i\delta(\mathbf{r}-\mathbf{r}_i) , \tag{74}$$

and η is a positive constant. The solution of Eq. (71) is then

$$\theta_1(\mathbf{r}) = -\frac{1}{2\pi}\sum_{i=1}^{N} B_i \int \frac{e^{-\frac{k^2}{4\eta}}}{k^2} e^{i\mathbf{k}\cdot(\mathbf{r}_i-\mathbf{r})} d\mathbf{k} . \tag{75}$$

Similarly, the solution of Eq. (72) is

$$\theta_2(\mathbf{r}) = \sum_{i=1}^{N} B_i \ln|\mathbf{r}-\mathbf{r}_i| - \frac{\eta}{\pi}\sum_{i=1}^{N} B_i \int \ln|\mathbf{r}-\mathbf{r}'| e^{-\eta|\mathbf{r}'-\mathbf{r}_i|^2} d\mathbf{r}' , \quad (76)$$

which can be reduced to (see Appendix B)

$$\theta_2(\mathbf{r}) = -\sum_{i=1}^{N} B_i \int_{|\mathbf{r}-\mathbf{r}_i|}^{\infty} \frac{e^{-\eta r'^2}}{r'} dr' . \quad (77)$$

Combining Eqs. (75) and (77), we obtain

$$\theta(\mathbf{r}) = B_0 - \frac{1}{2\pi}\sum_{i=1}^{N} B_i \int \frac{e^{-\frac{k^2}{4\eta}}}{k^2} e^{i\mathbf{k}\cdot(\mathbf{r}_i-\mathbf{r})} d\mathbf{k} - \sum_{i=1}^{N} B_i \int_{|\mathbf{r}-\mathbf{r}_i|}^{\infty} \frac{e^{-\eta r'^2}}{r'} dr' . \quad (78)$$

A tractable form of Eq. (70) can then be found using Eqs. (67), (78), and (70) (see Appendix C). This form is

$$\frac{1}{R_j} = B_0 + B_j\left[\ln(R_j/L) + \int_0^1 \frac{1-e^{-r'^2}}{r'} dr' - \int_1^{\infty} \frac{e^{-r'^2}}{r'} dr'\right] - \sum_{i=1, i\neq j}^{N} B_i \int_{|\mathbf{r}_j-\mathbf{r}_i|/L}^{\infty} \frac{e^{-r'^2}}{r'} dr' - \frac{2\pi}{L^2}\sum_{i=1}^{N} B_i \sum_{\mathbf{k}\neq 0} \frac{e^{-k^2/4L^2}}{k^2} e^{i\mathbf{k}\cdot(\mathbf{r}_i-\mathbf{r}_j)}, \quad (79)$$

where L is the system size.

The basic equations used to simulate two-dimensional Ostwald ripening are the conservation law Eq. (18), Eq. (79), and the two-dimensional version of Eq. (21).

V. RESULTS OF NUMERICAL SIMULATION

The most time-consuming step in the simulation is the calculation of the growth rates $\{B_i\}$, which is computationally of order N^3 (except for $D = 3$ with $\phi = 0$). For each independent run, we iterate about N times; therefore, each run costs of the order of N^4 numerical manipulations. In addition, to prevent numerical instability, we utilized double precision in our simulations. As a result, it is expensive for large-scale simulations. In the present work, we used about 1000 CPU hours on an IBM 3090 computer.

Our approach is essentially the same as that of VG, although we study much larger systems, with therefore many more interactions. In Beenakker's simulation,[8] he only included a small number (about 20) of nearest-neighbor iterations to save computer time. This implied that the growth rate $\{B_i\}$ did not globally satisfy the conservation law, Eq. (18), which resulted in a volume fraction drift of 10–20 %. This drift also resulted from his time increment: His algorithm allowed more than one droplet to be shrunk in a single iteration. Thus, some droplets could have a negative volume when they were removed from the system. From our tests, his algorithm cannot give consistent results unless at least 100 nearest-neighbor interactions are included. In the present work, we have included all the interactions.

Our numerical simulations were conducted as follows. The system was initialized by randomly generating a set of $\{R_i\}$ consistent with the distribution function of our analytical calculation [i.e., Eq. (57)], and randomly distributing this set of droplets without overlap. A variety of initial conditions were examined, all of which led to the same asymptotic distribution function. After setting the initial radii and locations of the droplets, Eqs. (18) and (66) for three dimensions [(79) for two dimensions] were solved to obtain values for $\{B_i\}$. Equation (21) was then used to obtain a new set of $\{R_i\}$ after a small time increment. The procedure was then iterated. In order to keep the volume fraction constant during the iterations, the time increment was determined self-consistently by shrinking, at most, one droplet in each single time step. Thus, the volume fraction did not change except by numerical roundoff. This self-consistent determination of time is the only way we have found to keep the volume fraction from drifting. Moreover, for a given volume fraction the droplet radii $\{R_i\}$ and the distances between droplets $\{|\mathbf{r}_i - \mathbf{r}_j|\}$ are proportional to the system L; therefore, the simulation results do not depend on the system size L if the time increment is proportional to L^3.

First of all, we carried out the simulation for $D = 3$ and $\phi = 0$ to test our algorithm. In this case, $|\mathbf{r}_i - \mathbf{r}_j| \to \infty$, and the third term on the right-hand side of Eq. (66) vanishes. As a result, Eq. (66) becomes so simple that we can perform extremely-large-scale simulation. We

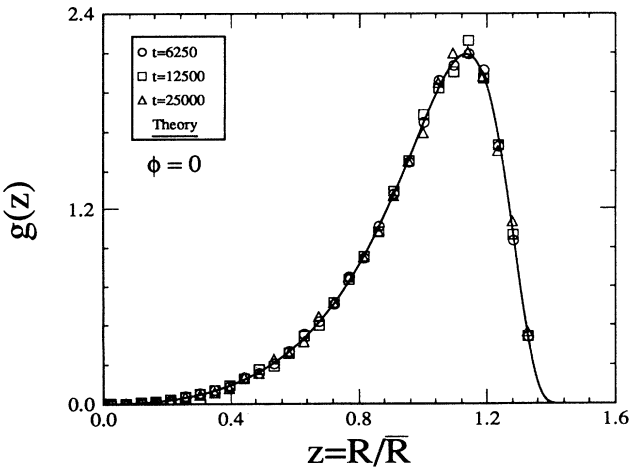

FIG. 5. Predictions of our numerical simulation for scaled normalized distribution $g(z)$ vs scaled droplet radius $z = R/\overline{R}$, in $D = 3$ and $\phi \to 0$. The solid line is Eq. (13), and the different symbols correspond to simulation results at different time steps of the iterations.

started with 50 000 droplets and then iterated until the number of droplets was reduced to 25 000. In each iteration, only one droplet was shrunk. The scaled distribution function, the time evolutions of both the average droplet radius and the total number of droplets have been plotted in Figs. 5, 6, and 7, respectively. In Fig. 5, the solid line is Eq. (57) for $D = 3$ and $\phi \to 0$; the different symbols correspond to different times. All the symbols lying on the same universal solid line confirm the scaling behavior of distribution function [Eq. (35)]. Figures 6(a) and 7(a) show that our numerical results give $\overline{R}(t) = [\overline{R}^3(0) + K(\phi)t]^{1/3}$ and $N(t) = N(0)\overline{R}^3(0)/[\overline{R}^3(0) + K(\phi)t]$, respectively, which are the same as Eqs. (58) and (59). A check on our numerics is provided by comparing the values of $K(0)$ obtained from R or N. From Figs. 6 and 7, we obtained $K(0) = 0.4442$ and $K(0) = 0.4434$, from R and N, respectively. The relative difference between these independent measurements is about 0.2%. Comparing to the theoretical result, $4/9 \simeq 0.4444$, the relative difference is less than 0.3%, much better than that of earlier work on small systems.[7]

Except for $D = 3$ and $\phi = 0$, all systems were initialized with 1000 droplets and iterated until the total number of droplets was reduced to approximately 300. Fifty independent sets of initial conditions were averaged for $D = 3$ with $\phi = 0.01$ and 0.05; and $D = 2$ with $\phi = 0.01$, 0.05, and 0.10. For $D = 3$ and $\phi = 0.10$, 12 independent runs with different initial conditions were carried out; for other parameters, 5 independent runs were performed. The dynamic growth exponent was measured by examining both the average droplet size and the total number of droplets. In Figs. 6 and 7, $\overline{R}$ and N are plotted, respectively, for various volumes fractions. These figures indicate that the average radius obeys $\overline{R} = [\overline{R}^3(0) + K(\phi)t]^{1/3}$, and number of droplets

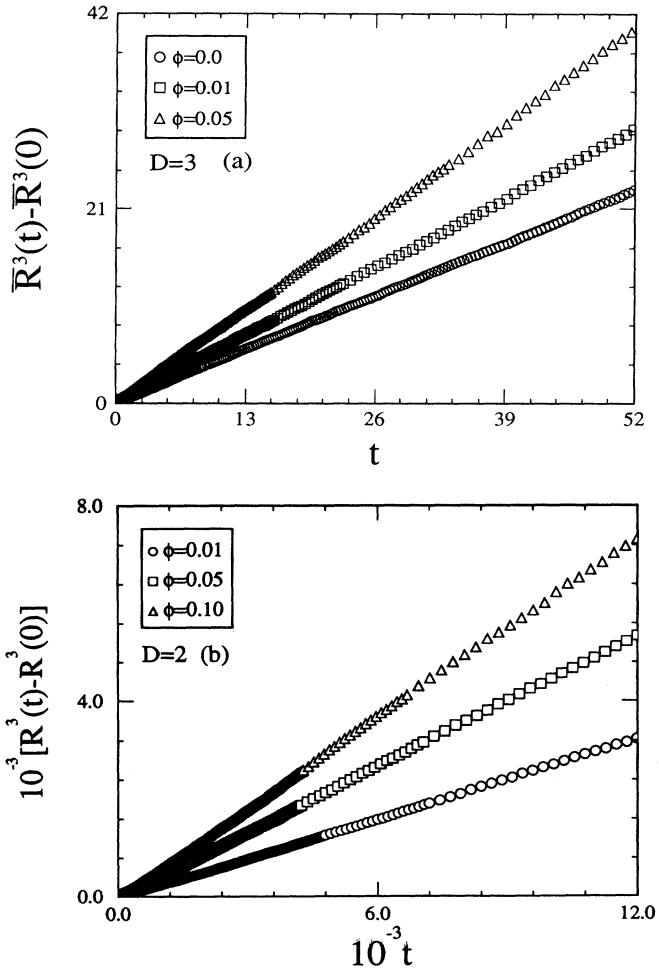

FIG. 6. Results of numerical simulations for the time evolution of average droplet size $[\overline{R}^3(t) - \overline{R}^3(0)$ vs $t]$ for $\phi = 0$, 0.01, and 0.05 in $D = 3$ (a); for $\phi = 0.01$, 0.05, and 0.10 in $D = 2$. The straight lines indicate that the time evolution of the average droplet radius obeys $\overline{R}(t) = [\overline{R}^3(0) + K(\phi)t]^{1/3}$.

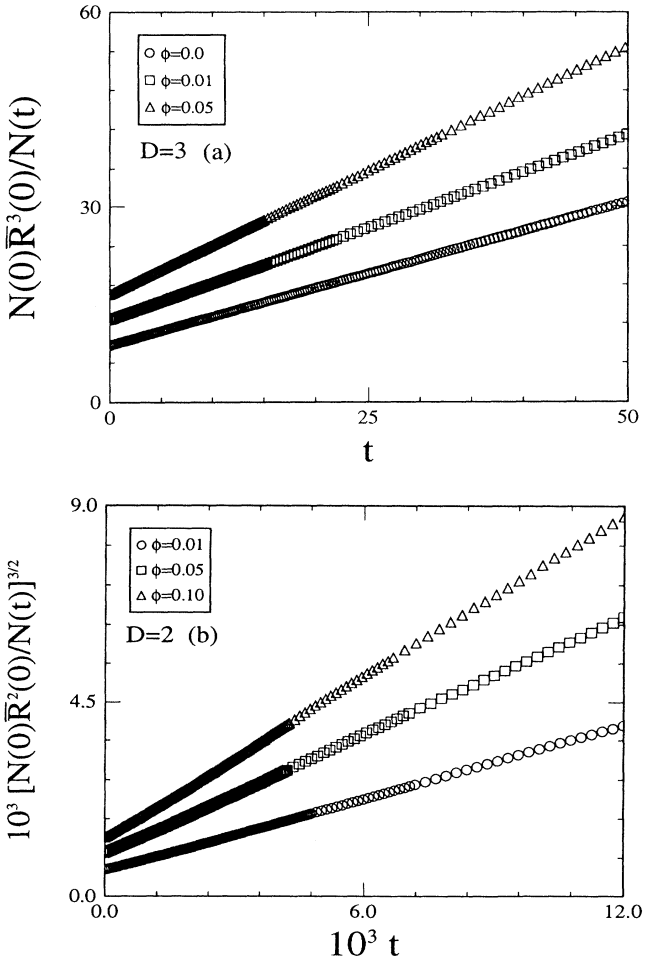

FIG. 7. Plots for $[N(0)\overline{R}^D(0)/N(t)]^{3/D}$ vs t for $\phi = 0$, 0.01, and 0.05 in $D = 3$ (a); for $\phi = 0.01$, 0.05, and 0.10 in $D = 2$ (b). The straight lines indicate that the time evolution of the number of the droplets satisfies $N(t) = N(0)\overline{R}^D(0)/[K(\phi)t + \overline{R}^3(0)]^{D/3}$.

satisfies $N(t) = N(0)\overline{R}^D(0)/[K(\phi)t + \overline{R}^3(0)]^{D/3}$. Both these results are consistent with our theoretical predictions, Eqs. (58) and (59). The relative difference between these two independent measurements for $K(\phi)$ are about 1% (except for $D = 3$ and $\phi = 0$). The relative errors for K are from 0.2% to 1%. The values for the coarsening rate obtained by the above fits are shown as a function of ϕ in Figs. 8(a) and 8(b), in which the numerical values for K are compared with various theoretical calculations. The numerical values of K are much closer to our theoretical prediction than the other two- and three-dimensional theories.

Comparisons of our prediction for $g(z)$ and $D = 3$ with the simulations, an experimental result,[21] and other theories are shown in Figs. 9(a) and 9(b). The different symbols correspond to distribution functions at different times. All these symbols lying on the same line confirm our theoretical prediction, Eq. (35). Our prediction is much closer to the simulation and the experimental results than the other theories, although the precision of experimental data is not sufficient to provide a strong test for theory.

The above comparison shows that higher-order volume fraction effects are very important for K. For example, Fig. 8(a) indicates that, for $\phi > 0.01$, the perturbatively calculated coarsening rate of MR and TKE differ significantly from ours, even though our results are the same as theirs up to order of $\mathcal{O}(\sqrt{\phi})$. The results of Figs. 3, 8(a), 9(a), and 9(b) indicate that higher-order volume fractions are important even for small ϕ.

The scaled distribution function, $g(z)$, in $D = 2$ is dis-

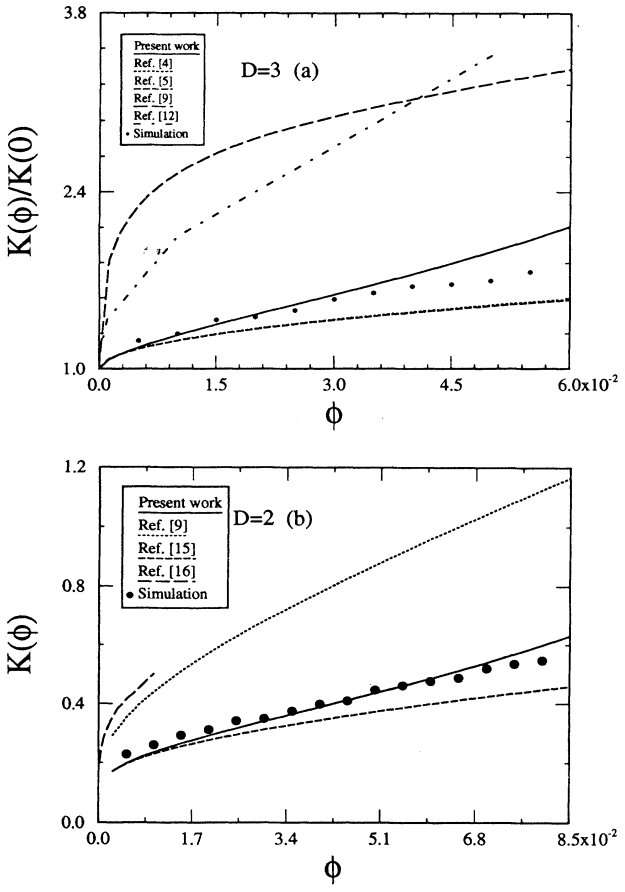

FIG. 8. Plots for the coarsening rates vs ϕ in both $D = 3$ (a) and $D = 2$ (b). In (a) $[K(\phi)/K(0)$ vs $\phi]$, the dotted, dashed, long-dashed, dot-dashed, and solid lines correspond, respectively, to the $D = 3$ results of MR (Ref. 4), TKE (Refs. 5 and 6), Ardell (Ref. 9), Mardar (Ref. 12), and ours. The lines for MR and TKE are almost superimposed. The symbols correspond to the simulation results. In (b) $[K(\phi)$ vs $\phi]$, dotted, dashed, long-dashed, and solid lines correspond, respectively, to the $D = 2$ results of Ardell (Ref. 9), MR (Ref. 4), ZG (Ref. 16), and ours. The symbols represent the simulation results.

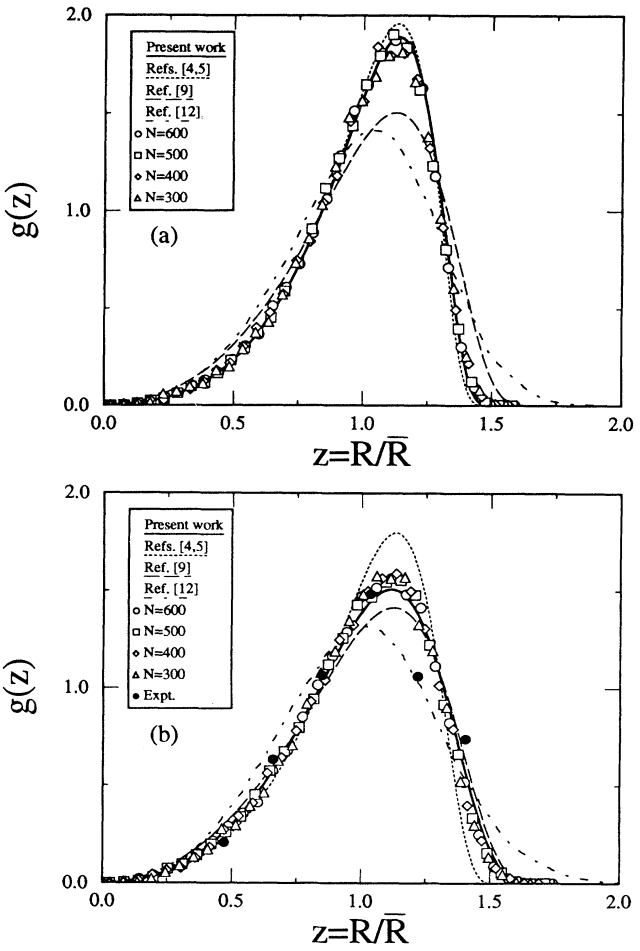

FIG. 9. Comparisons of the distribution functions $g(z)$ with other theories, the simulations, and an experiment is displayed in $D = 3$ for $\phi = 0.01$ in (a); for 0.05 in (b). The symbols (except the solid circles) are the simulation results. The different symbols correspond to different times at which the number of remaining droplets, $N \simeq 600$, 500, 400, and 300. The dotted, long-dashed, dot-dotted, and solid lines are the respective predictions of MR (Ref. 4), TKE (Ref. 5), Ardell (Ref. 9), Mardar (Ref. 12), and ours [i.e., Eq. (57) in $D = 3$], where the lines for MR and TKE are superimposed. In (b), the solid circle is the experimental distribution function at very late times (Ref. 21) for $\phi \sim 0.05$.

played in Figs. 10(a) and 10(b) for $\phi = 0.01$ and 0.05, respectively, at several different times. The collapse of the data to a single curve $g(z)$ for several different times is consistent with the scaling relationship given in Eq. (35). The numerical results are also compared to our calculations and those of other theories.[22] Overall, our theoretical predictions for $g(z)$ and $K(\phi)$ compare very well to the numerical simulation. However, it is apparent that the distribution function determined by Ardell[9] provides the best fit of the numerical results, although the values of K predicted by his theory are incompatible with the numerical determined ones. In a previous paper,[13] we presented his prediction for the distribution function, by choosing the free parameter in his theory such that the numerical coarsening rate agreed with his estimation. This procedure leads to a bad fit for the distribution function. Thus the theory of Ardell cannot consistently fit the numerical results. In conclusion, overall, our theoretical results in both two and three dimensions conform to the large-scale simulations much better than any other theories. Moreover, we are aware that our results are also in good agreement with a nonlinear Langevin simulation by Toral, Chakrabarti, and Gunton,[18] although their results are not as accurate as those of our simulations.

In order to compare with previous simulations, we carried out 12 independent runs with different initial conditions for $\phi = 0.10$ in $D = 3$. For this simulation, $K(0.10) = 0.912 \pm 0.003$, whereas VG found $K(0.10) = 0.69 \pm 0.03$, and Beenakker found $K = 0.88$ for ϕ between 0.10 and 0.12. We think that these earlier studies involved systems of too small a size, and in Ref. 8, too small a range of interaction to obtain conclusive results as mentioned above.

The scaling behavior of the growth process can also be seen in the dynamic structure factor $S(k,t)$. The structure factor is defined to be $S(k,t) \equiv \sum_{\hat{k}} |\delta\theta(\mathbf{k},t)|^2 / \sum_{\hat{k}}$, where $\delta\theta \equiv \theta - \overline{\theta}$ and the sum is over a spherical shell. The assumption that all lengths scale with the same dy-

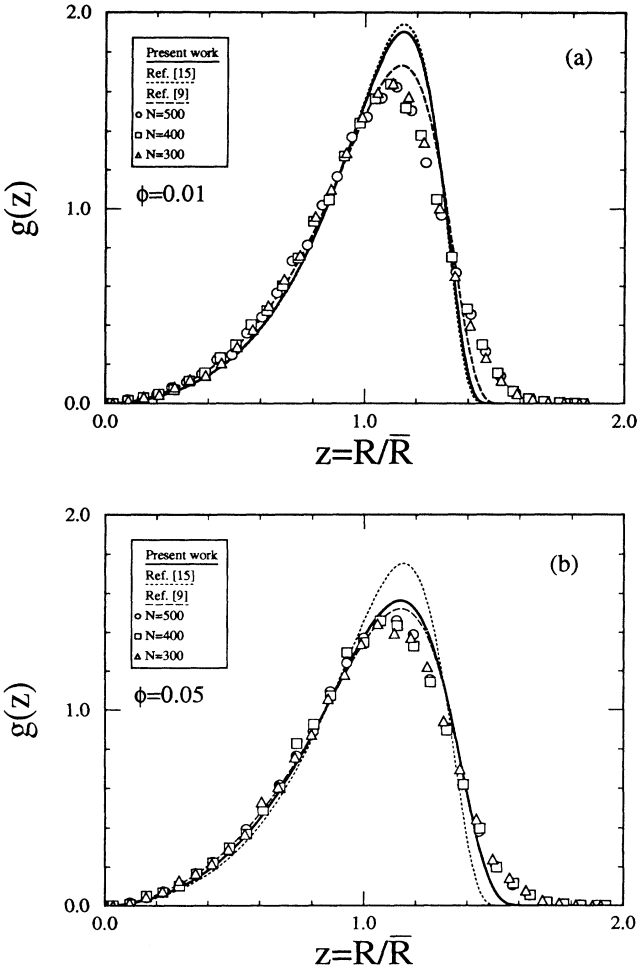

FIG. 10. Plot of the scaled normalized distribution function $g(z)$ vs the scaled radius $z = R/\overline{R}$ for $D = 2$. Dotted, dashed, and solid lines correspond, respectively, to Marqusee (Ref. 15), Ardell (Ref. 9), and ours [Eq. (57)]. Circles, squares, and triangles give the scaled normalized distribution functions from the simulation, corresponding, respectively, to different times at which the number of remaining droplets, $N \simeq 500$, 400, and 300, for $\phi = 0.01$ in (a); for $\phi = 0.05$ in (b).

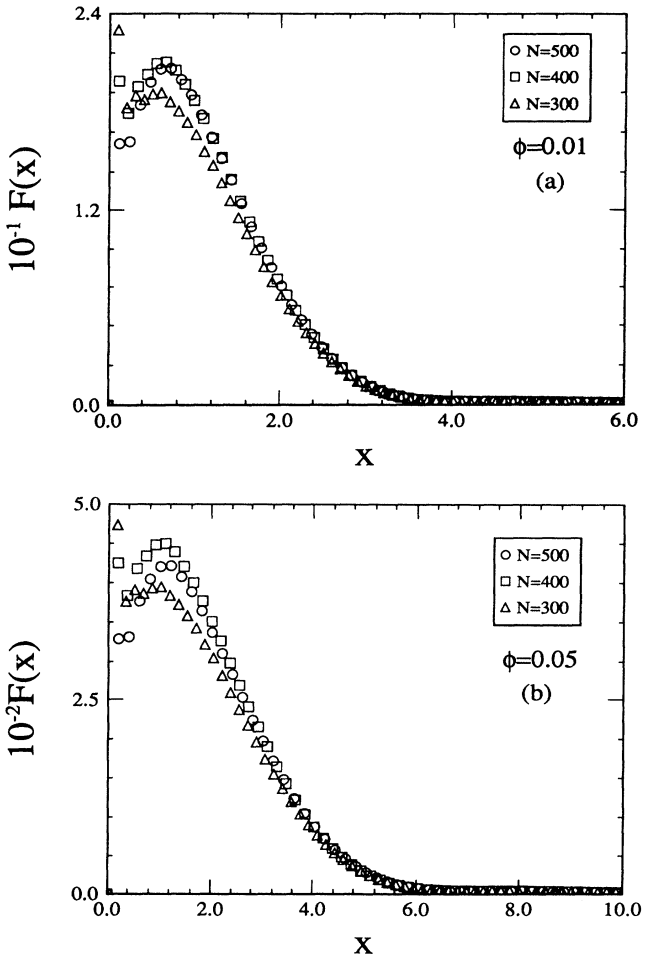

FIG. 11. Scaled structure factor $F(x)$ in $D = 3$ is shown as a function of x for $\phi = 0.01$ and 0.05 in (a) and (b), respectively.

namic exponent leads to the following relationship:[3]

$$S(k,t) = \overline{R}^D F(k\overline{R}) \ , \tag{80}$$

where $F(x)$ is the scaling function. This is an important quantity which can be measured directly in experiment.

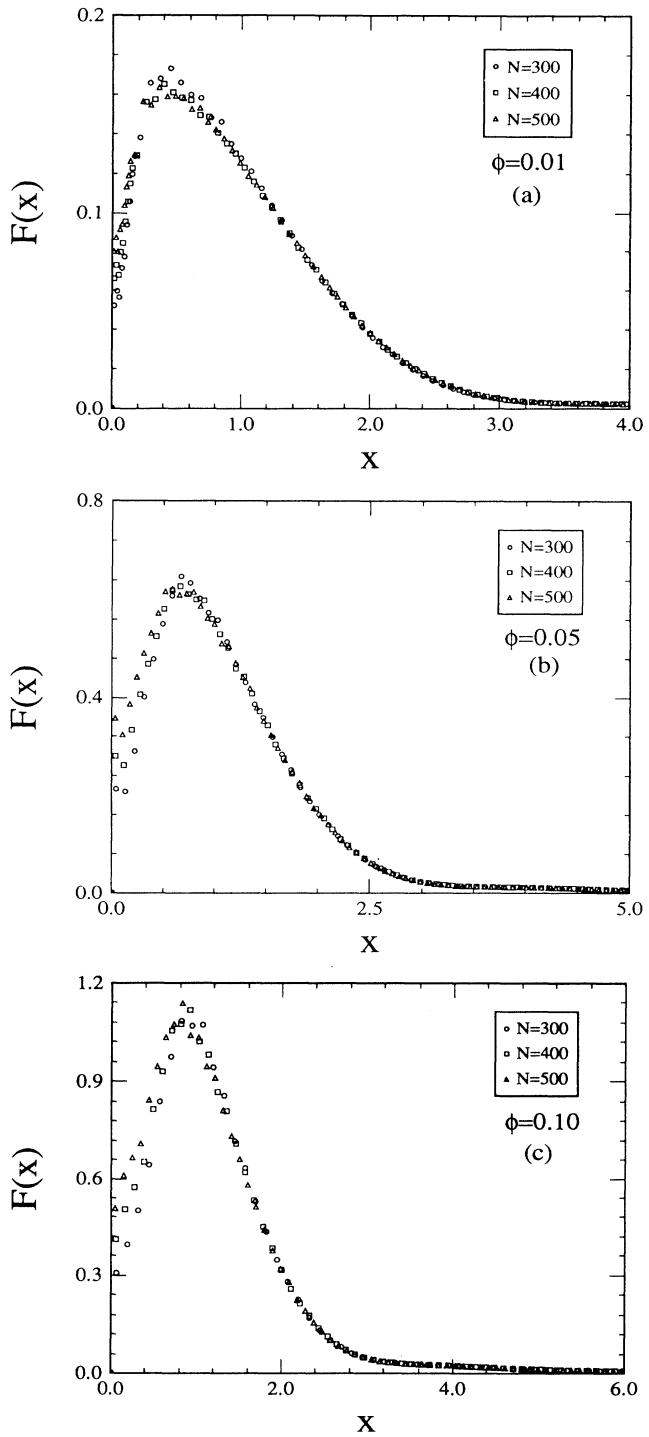

FIG. 12. Scaled structure factor $F(x)$ in $D = 2$ is shown as a function of x for $\phi = 0.01$, 0.05, and 0.10 in (a), (b), and (c), respectively.

For simplicity, in the calculation of the structure factor, we set $\theta = 1$ and -1 inside and outside of the droplets, respectively, and $L^3 = 120^3$ for $D = 3$; $L^2 = 1024^2$ for $D = 2$. For $D = 3$, Figs. 11(a) and 11(b) show $F(x)$ vs x for $\phi = 0.01$ and 0.05, respectively, at three different times. In Figs. 12(a), 12(b), and 12(c), $F(x)$ is displayed for $\phi = 0.01$, 0.05, and 0.10, respectively, at several different times in $D = 2$. The time independence of $F(x)$ indicates the scaling prediction is quite good. For small x, $F(x)$ does not scale well due to finite-system-size effects; i.e., the longest distance among the droplets cannot be scaled by the average droplet radius. Apparently, two-dimensional finite-size effects are smaller that those of three dimensions. A similar shape for the two-dimensional scaling function for small ϕ has been reported recently by Chakrabarti, Toral, and Gunton,[18] who numerically solved a Langevin model for Ostwald ripening. The large x dependence of $F(x)$ is shown in Fig. 13. These figures indicate that our numerical results for $F(x)$ are in good agreement with Porod's law, i.e., $F(x) \sim 1/x^{D+1}$.

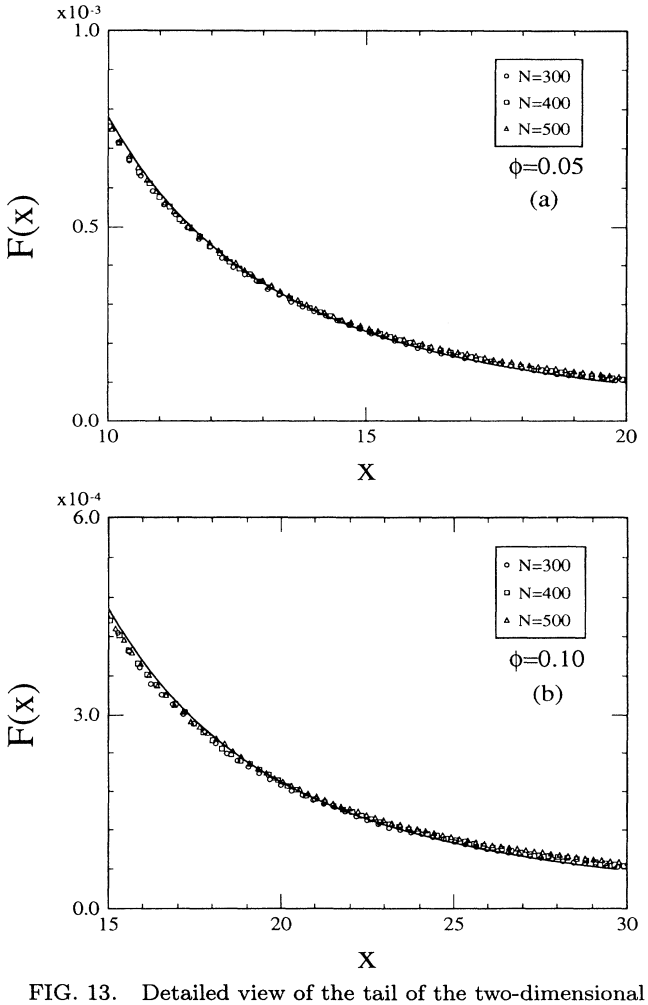

FIG. 13. Detailed view of the tail of the two-dimensional scaled structure factor $F(x)$ for $\phi = 0.05$ and in (a), and $\phi = 0.10$ in (b). The solid line in (a) is $F(x) = 0.78/x^3$; the solid line in (b) is $F(x) = 1.58/x^3$.

VI. CONCLUSION

In conclusion, the present article has developed a theory for Ostwald ripening for $D \geq 2$ where screening effects due to interacting droplets are incorporated. The solution of these mean-field equations gives the coarsening rate, the time evolution of the total number of droplets, and the droplet-distribution function. Within the mean-field model all order of ϕ are included, unlike earlier perturbative theories. Comparisons with both numerical and experimental results (in three dimensions) indicate that our approach more accurately describes the phenomenon of Ostwald ripening than previous work. The simulations also allowed us to study the scaled structure factors, indicating that the average droplet radius is the only length scale in the systems. In addition, the fundamental scaling behavior of droplet growth was obtained in both the analytic and numerical studies presented in this paper. We also note that our method can be extended to other physical systems, such as exciton[23,14] systems in semiconductors and microemulsions.[24,14]

Although the predictions of our mean-field theory conform well to our large-scale simulation and an experiment in three dimensions, the problem of Ostwald ripening remains open for very large volume fraction of droplets. In the future, it would be useful to develop a non-mean-field approach to Ostwald ripening in order to investigate that limit.

ACKNOWLEDGMENTS

We would like to thank Zaven Altounian for helpful discussions. This work was supported by the Natural Sciences and Engineering Research Council of Canada and le Fonds pour la Formation de Chercheurs et l'Aide à la Recherche de la Province de Québec.

APPENDIX A

If $w(x,\lambda) \neq 0$, then the Taylor expansion of $w(x,\lambda)$ at the point $x = x_0$ satisfies

$$w(x,\lambda) = w'(x_0,\lambda)(x-x_0)+\frac{w''(x_0,\lambda)}{2!}(x-x_0)^2+\cdots . \tag{A1}$$

Thus, the asymptotic behavior of $G(x)$ as $x \to x_0^-$ will be

$$\lim_{x\to x_0^-} G(x) = \frac{-D\lambda}{w'(x_0,\lambda)}(x-x_0)^{\frac{D\lambda}{w'(x_0,\lambda)}-1} . \tag{A2}$$

Therefore, when $D\lambda/w'(x_0,\lambda) - 1 \leq m < D\lambda/w'(x_0,\lambda)$,

$$\lim_{x\to x_0^-} G^{(m)}(x) \neq \lim_{x\to x_0^+} G^{(m)}(x) \tag{A3}$$

according to Eq. (46), and so $G(x)$ is not analytic at x_0.

APPENDIX B

Integrating Eq. (76) by parts leads to the following equation:

$$\theta_2(\mathbf{r}) = \sum_{i=1}^{N} B_i \ln|\mathbf{r}-\mathbf{r}_i| + \frac{1}{4\pi}\sum_{i=1}^{N} B_i \int \ln[r'^2+(\mathbf{r}-\mathbf{r}_i)^2 - 2r'|\mathbf{r}-\mathbf{r}_i|\cos\theta]e^{-\eta r'^2}|_0^\infty d\theta$$

$$-\frac{1}{4\pi}\sum_{i=1}^{N} B_i \int e^{-\eta r'^2}\frac{2(r'-|\mathbf{r}-\mathbf{r}_i|\cos\theta)}{r'^2+(\mathbf{r}-\mathbf{r}_i)^2-2r'|\mathbf{r}-\mathbf{r}_i|\cos\theta}d\theta\, dr' . \tag{B1}$$

The first term and second term in Eq. (B1) cancel each other; therefore,

$$\theta_2(\mathbf{r}) = -\frac{1}{2\pi}\sum_{i=1}^{N} B_i \int \frac{(r'-|\mathbf{r}-\mathbf{r}_i|\cos\theta)e^{-\eta r'^2}d\theta\, dr'}{r'^2+(\mathbf{r}-\mathbf{r}_i)^2-2r'|\mathbf{r}-\mathbf{r}_i|\cos\theta} . \tag{B2}$$

The integral in the above expression can determined exactly to give Eq. (79).

APPENDIX C

Equation (70) can be rewritten as

$$\frac{1}{R_j} = B_0 + B_j \ln R_j + \lim_{\mathbf{r}'_j\to\mathbf{r}_j}\left[\sum_{i=1}^{N} B_i \ln|\mathbf{r}'_j-\mathbf{r}_i| - B_j \ln|\mathbf{r}'_j-\mathbf{r}_j|\right] . \tag{C1}$$

Comparing Eqs. (67), (78), and (C1), we obtain

$$\frac{1}{R_j} = B_0 + B_j \ln R_j + B_j \lim_{\mathbf{r}'_j \to \mathbf{r}_j} \left[\int_{|\mathbf{r}'_j - \mathbf{r}_j|}^{1} \frac{1}{r'} dr' - \int_{|\mathbf{r}'_j - \mathbf{r}_j|}^{\infty} \frac{e^{-\eta r'^2}}{r'} dr' \right] - \sum_{i=1, i\neq j}^{N} B_i \int_{|\mathbf{r}_j - \mathbf{r}_i|}^{\infty} \frac{e^{-\eta r'^2}}{r'} dr'$$
$$- \frac{1}{2\pi} \sum_{i=1}^{N} B_i \int \frac{e^{-\frac{k^2}{4\eta}}}{k^2} e^{i\mathbf{k}\cdot(\mathbf{r}_i - \mathbf{r}_j)} d\mathbf{k}$$
$$= B_0 + B_j \left(\ln R_j + \int_0^1 \frac{1 - e^{-\eta r'^2}}{r'} dr' - \int_1^{\infty} \frac{e^{-\eta r'^2}}{r'} dr' \right) - \sum_{i=1, i\neq j}^{N} B_i \int_{|\mathbf{r}_j - \mathbf{r}_i|}^{\infty} \frac{e^{-\eta r'^2}}{r'} dr'$$
$$- \frac{1}{2\pi} \sum_{i=1}^{N} B_i \int \frac{e^{-\frac{k^2}{4\eta}}}{k^2} e^{i\mathbf{k}\cdot(\mathbf{r}_i - \mathbf{r}_j)} d\mathbf{k} \,. \tag{C2}$$

After making a transformation $\sqrt{\eta} r' = t$, we can write Eq. (C2) as

$$\frac{1}{R_j} = B_0 + B_j \left[\ln(R_j \sqrt{\eta}) + \int_0^1 \frac{1 - e^{-r'^2}}{r'} dr' - \int_1^{\infty} \frac{e^{-r'^2}}{r'} dr' \right] - \sum_{i=1, i\neq j}^{N} B_i \int_{\sqrt{\eta}|\mathbf{r}_j - \mathbf{r}_i|}^{\infty} \frac{e^{-r'^2}}{r'} dr'$$
$$- \frac{1}{2\pi} \sum_{i=1}^{N} B_i \int \frac{e^{-\frac{k^2}{4\eta}}}{k^2} e^{i\mathbf{k}\cdot(\mathbf{r}_i - \mathbf{r}_j)} d\mathbf{k} \,. \tag{C3}$$

Setting $\eta = L^{-2}$, where L is the system size, and using toroidal boundary conditions, Eq. (C3) becomes

$$\frac{1}{R_j} = B_0 + B_j \left[\ln(R_j / L) + \int_0^1 \frac{1 - e^{-r'^2}}{r'} dr' - \int_1^{\infty} \frac{e^{-r'^2}}{r'} dr' \right] - \sum_{i=1, i\neq j}^{N} B_i \int_{|\mathbf{r}_j - \mathbf{r}_i|/L}^{\infty} \frac{e^{-r'^2}}{r'} dr'$$
$$- \frac{2\pi}{L^2} \sum_{i=1}^{N} B_i \sum_{\mathbf{k}\neq 0} \frac{e^{-k^2/4L^2}}{k^2} e^{i\mathbf{k}\cdot(\mathbf{r}_i - \mathbf{r}_j)} . \tag{C4}$$

The apparent singularity at $\mathbf{k} = \mathbf{0}$ is eliminated due to Eq. (18).

---

*Present address: Physics Department, Queen's University, Kingston, Ontario, Canada K7L 3N6.

[1] I. M. Lifshitz and V. V. Slyozov, J. Phys. Chem. Solids **19**, 35 (1961).

[2] C. Wagner, Z. Electrochem. **65**, 581 (1961).

[3] J. D. Gunton, M. San Miguel, and P. S. Sahni, in *Phase Transitions and Critical Phenomena*, edited by C. Domb and J. L. Lebowitz (Academic, London, 1983), Vol. 8.

[4] J.A. Marqusee and J. Ross, J. Chem. Phys. **80**, 536 (1984).

[5] M. Tokuyama and K. Kawasaki, Physica **123A**, 386 (1984); M. Tokuyama, K. Kawasaki, and Y. Enomoto, *ibid.* **134A**, 323 (1986); K. Kawasaki, Y. Enomoto, and M. Tokuyama, *ibid.* **135A**, 426 (1986); Y. Enomoto, M. Tokuyama, and K. Kawasaki, Acta Metall. **34**, 2119 (1986).

[6] Here, we only present the mean-field results of TKE, called the drift-term approximation by them. In our earlier paper (Ref. 13), we used an incorrect definition of the volume fraction given by TKE in Ref. 5. This resulted in an inaccurate calculation of their coarsening rate and the distribution function which is corrected here.

[7] P. W. Voorhees and M. E. Glicksman, Acta Metall. **32**, 2001 (1984); **32**, 2013 (1984); P. W. Voorhees, J. Stat. Phys. **38**, 231 (1985).

[8] C.W.J. Beenakker, Phys. Rev. A **33**, 4482 (1986).

[9] A. J. Ardell, Phys. Rev. B **41**, 2554 (1990); Acta Metall. **20**, 61 (1972).

[10] K. Tsumuraya and Y. Miyata, Acta Metall. **31**, 437 (1983).

[11] A.D. Brailsford and P. Wynblatt, Acta Metall. **27**, 489 (1979).

[12] M. Mardar, Phys. Rev. Lett. **55**, 2953 (1985); Phys. Rev. A **36**, 858 (1987). Mardar's theory includes spatial correlations which are absent from our approach. In principle, these effects are expected to become important for large volume fractions. However, his approach involves uncontrolled approximations such that, in our opinion, spatial correlations are not included systematically. Indeed, for nonzero volume fraction, there is no regime of agreement between his work and any other theory, or the numerical simulation presented herein.

[13] Some of these results have been previously published in a short paper: J. H. Yao, K. R. Elder, H. Guo, and M. Grant, Phys. Rev. B **45**, 8173 (1992).

[14] J. H. Yao, Ph.D thesis, McGill University, Canada, 1992.

[15] J.A. Marqusee, J. Chem. Phys. **81**, 976 (1984).

[16] Q. Zheng and J.D. Gunton, Phys. Rev. A **39**, 4848 (1989).

[17] T. M. Rogers and R. C. Desai, Phys. Rev. B **39**, 11 956 (1989).

[18] R. Toral, A. Chakrabarti, and J. D. Gunton, Phys. Rev. A **45**, 2147 (1992); A. Chakrabarti, R. Toral, and J. D. Gunton (unpublished).

[19] P. P. Ewald, Ann. Phys. (Leipzig) **64**, 253 (1921).

[20] Note that on using Eq. (21), we obtain the continuous version of Eq. (18), $\int_0^{\infty} d(vR^D)/dt f(R,t) dR = 0$. Therefore, $\partial \theta_{av} / \partial t = 0$; i.e., from the conservation law, Eq. (18), the total amount of solute in the majority phase remains constant.

[21]K. Rastogi and A.J. Ardell, Acta Metall. **19**, 321 (1971).
[22]Because Zheng and Gunton did not present the distribution function for $\phi = 0.01$ or $\phi = 0.05$, we are not able to compare with their results.
[23]J. H. Yao, H. Guo, and M. Grant, Phys. Rev. B **47**, 1270 (1993).
[24]J. H. Yao and M. Laradji (unpublished).